

Antimonene with Topological Nontrivial Band Structure on Al(111) Substrate

Yang Wang^{1,†,*}

AFFILIATIONS

¹*Department of Physics, Hebei Normal University, Shijiazhuang 050024, China*

E-mail: 161842340@masu.edu.cn

Abstract

Large-area, high-quality monocrystalline antimonene polygons without alloy layers have been spontaneously synthesized on an Al(111) substrate at room temperature. Experimental measurements and first-principles calculations both reveal a Dirac point at the Γ point near -1.4 eV in antimonene on Al(111), confirming that the structure exhibits topologically nontrivial properties. Additionally, a previously unpredicted kagome lattice structure of antimonene has been discovered, leading to a low-dispersion band structure near the Fermi level, which has significant implications for electronic properties and transport characteristics. These findings hold great potential for the next generation of electronic devices due to the material's distinctive electron transport properties and spin characteristics. Furthermore, first-principles calculations are utilized to verify the interaction forces between atoms in the Sb structure.

Keywords: β -antimonene, kagome, Dirac cone, flat band

1. Introduction

Two-dimensional (2D) crystals are a unique class of materials that are significantly thinner than traditional crystalline substances and possess periodic structures without free surface bonds. Graphene, as a prominent 2D material, has garnered significant attention due to its extraordinary properties, prompting extensive exploration of other 2D materials with similar rotational symmetry [1-4]. Group-V elemental monolayers [5], such as black and blue phosphorene [6, 7], arsenene, antimonene [8, 9] and bismuthene [10], have been extensively studied. In particular,

antimonene has attracted considerable academic interest due to its tunable band gap [8].

The stability of antimonene in both α and β phases has been confirmed through phonon dispersion calculations [11]. Antimonene can be synthesized through various methods; for example, β -phase antimonene polygons can be grown on mica substrates via van der Waals epitaxy without forming an alloy layer [12]. Furthermore, both α -Sb and β -Sb have been successfully fabricated on Ag(111) [13], Cu(111) [14], and Au(111) substrate [15] using molecular beam epitaxy (MBE).

However, when antimonene is overlaid on surfaces covered with an alloy layer [16, 17] on these noble metal substrates, some novel properties may be lost. This is significant because freestanding β -Sb has been theoretically predicted, via density functional theory (DFT), to be a two-dimensional topological insulator at critical buckling angles [18] or lattice constant [19] by the density functional theory (DFT). However, this prediction lacks experimental confirmation. The boundary states of a topological insulator are characterized by the presence of Dirac cones [20], which hold great potential for the next generation of electronic devices due to their high conductivity. Yet, among all 2D materials, only the Dirac cones in graphene have been reliably confirmed experimentally thus far [2].

Another special electronic structure, known as the flat band (FB), exhibits dispersionless characteristics in momentum space and possesses many interesting properties [21]. The FB can theoretically be achieved in a kagome lattice [22], a rare structure composed of opposing triangular lattices and considered a deformation of the honeycomb lattice. Silicon (Si), germanium (Ge), and antimony (Sb) are adjacent elements in the periodic table, kagome lattices of germanene and silicene exhibiting FB structures have been fabricated on Al(111) substrates [23, 24]. Additionally, germanene with a honeycomb lattice has also been fabricated on an Al(111) substrate without forming an alloy layer [25].

Inspired by prior pioneering research, we present the first successful synthesis of β -Sb on an Al(111) substrate without forming an alloy layer. Additionally, we report the first observation of antimonene adopting a kagome lattice, a structure that had not

been predicted before. Through our experiments, we measured a Dirac node at the Γ point near -1.4 eV and provided the first experimental demonstration of antimonene as a topological insulator, with corresponding DFT calculations further validating our experimental observations. Furthermore, we confirmed the presence of a flat band (FB) in kagome phase, and theoretically elucidated the nature of the interactions.

2. Experimental section

The unit cell of single-crystal aluminum is face-centered cubic (FCC) with a lattice constant of 4.04Å. The Al(111) surface exhibits hexagonal symmetry with a 1×1 surface reconstruction [26], as shown in Fig. 1d, which ensures that structures deposited on this surface via MBE are also single-crystalline. The Al(111) substrate was cleaned through cycles of Ar^+ sputtering and annealing at 550°C. The resulting smooth and extended substrate surface was observed using scanning tunneling microscopy (STM) [27], as depicted in Fig. 1c. STM measurements were conducted at 77 K under ultra-high vacuum conditions (1×10^{-10} mbar) using a Createc STM system. The acquired STM images were processed using WSxM software. Based on the height profiles, no impurity islands or vacancies were observed on the substrate surface after annealing. Consequently, sharp diffraction patterns were observed using reflection high-energy electron diffraction (RHEED), as shown in Figs. 1a and 1b. The two diffraction patterns correspond to incident electron beams at angles differing by 30°. According to the zone law, the RHEED diffraction patterns provide insights into the reciprocal lattice [28], indicating that the $[1\bar{1}0]$ and $[2\bar{1}\bar{1}]$ crystal orientations correspond to the narrow and wide streaks, respectively, in Figs. 1a and 1b.

Once a clean Al(111) substrate was obtained, Sb atoms were evaporated from an effusion cell [29]. The temperature of the Sb source displayed on the control panel, was maintained at 350°C. The growth chamber of the MBE system is maintained at room temperature under ultra-high vacuum conditions (1×10^{-10} mbar). This study focuses on investigating the evolution of the Sb atomic structure during an 10-minute deposition process to ensure the growth of a well-crystallized Sb epitaxial layer. STM

results of Sb atoms deposited on Al(111) are shown in Figs. 1g–1j. Although various ordered structures formed spontaneously during deposition, only one distinct RHEED diffraction pattern was observed, as shown in Figs. 1e and 1f.

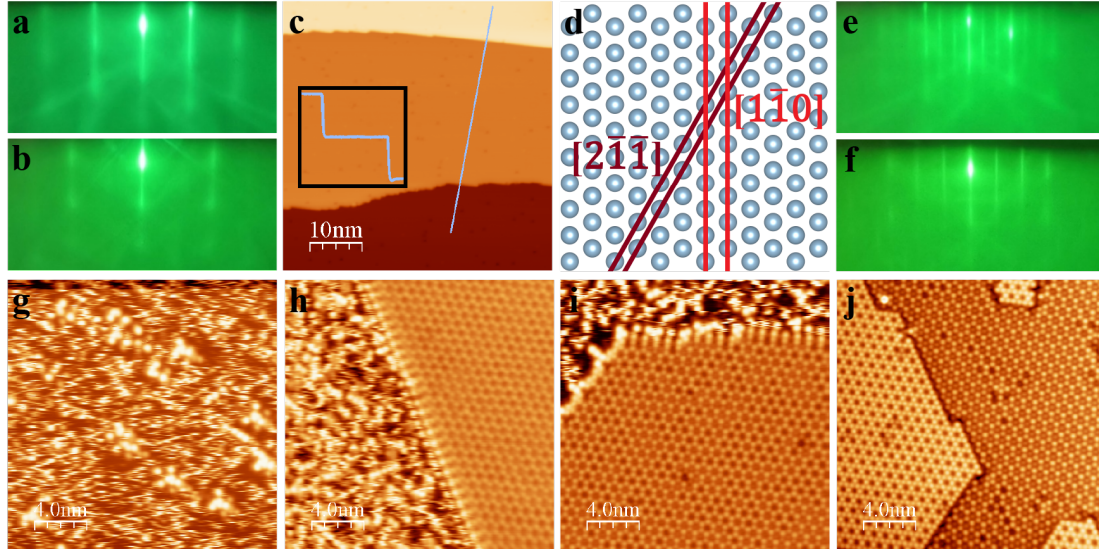


Figure. 1. Experimental process applied to the Al(111) substrate which presents high-resolution STM images that depict the evolution of surface topography over time and RHEED diffraction patterns. (a and b) RHEED diffraction pattern of Al(111) surface along the crystal orientation of $[1\bar{1}0]$ and $[2\bar{1}\bar{1}]$ respectively. (c) $50\text{nm}\times 50\text{nm}$ large scale STM image of Al(111) substrate with $V_b=1\text{V}$ and $I_t=100\text{pA}$. Inset: A height profile along the blue line at the terrace edge, the height corresponds to the intrinsic height of Al(111) terrace is around 2.5pm . (d) The model of aluminum single crystal in the section of (111) plane. (e and f) New diffraction pattern along $[1\bar{1}0]$ and $[2\bar{1}\bar{1}]$ respectively. (g) $20\text{nm}\times 20\text{nm}$ STM image with $V_b=0.5\text{V}$ and $I_t=500\text{pA}$ for 2 min deposition. (h) $20\text{nm}\times 20\text{nm}$ STM image with $V_b=0.4\text{V}$ and $I_t=500\text{pA}$ for 4 min deposition. (i) $20\text{nm}\times 20\text{nm}$ STM image with $V_b=0.5\text{V}$ and $I_t=600\text{pA}$ for 6 min deposition. (j) $20\text{nm}\times 20\text{nm}$ STM image with $V_b=0.5\text{V}$ and $I_t=310\text{pA}$ for 8 min deposition.

During the initial stages of deposition (≤ 2 min), Sb atoms existed as discrete clusters on the substrate. At this stage, the interaction between Sb atoms and the outermost Al atoms was comparatively weaker than the interaction among Sb atoms

themselves. As a result, Sb atoms exhibited an affinity to aggregate and could not form a two-dimensional structure. With the deposition time extended to 4 minutes, the observed RHEED patterns shown in Fig. 1e and 1f signified the emergence of a honeycomb lattice structure, marking the transition from a disordered Sb arrangement to an organized phase. This honeycomb lattice structure spontaneously formed at room temperature, and a clear demarcation was discernible between the disordered region and the honeycomb lattice, as shown in Figs. 1h and 1i. Notably, the atomic edge structure of the honeycomb lattice is neither zigzag nor armchair [30] but rather a special cubic edge structure. After 6 minutes of deposition, the previously vacant centers within the honeycomb structure became occupied by newly deposited Sb atoms. This resulted in a transition to a dice lattice structure, which consists of three equivalent sublattices, two of those sublattices form a honeycomb hexagonal structure, while the other is located at the center of each hexagon [31]. As illustrated in Figs. 1i and 1j, where both honeycomb and dice lattices coexist. Ultimately, at 8 minutes of deposition illustrated in Fig. 1j, a monolayer of island-like kagome lattice is stacked onto the dice lattice structure. Even after annealing the sample at the Al(111) substrate's annealing temperature, the observed RHEED patterns in Figs. 1d and 1e remained present, indicating the stability of antimonene on Al(111) as temperature increases. Changes in composition during deposition, as measured via X-ray photoelectron spectroscopy (XPS), are depicted in Fig. 2 and summarized in Table 1. The core-level spectra of Sb 4d [32] and Al 2p [33], obtained using an aluminum $K\alpha$ excitation source in XPS.

According to Fig. 2k, within the deposition time range of 1 to 10 minutes, the Sb atomic content increases as the deposition time extends. The binding energy initially shifts toward a lower value, then to a higher value, and finally shifts back to a lower value. This behavior indicates the emergence of different Sb components during the deposition process. Consequently, as the thickness of Sb atoms on the substrate surface increases, the signal intensity of the Al 2p peak detected by XPS correspondingly decreases, while the signal intensity of the Sb 4d peak enhances with longer deposition times, as shown in Fig. 2k. Notably, the binding energy of Al atoms

on the substrate surface remains unchanged throughout the deposition process. This finding further corroborates the conclusion drawn from previous STM measurements that no alloy formation occurs between Sb atoms and the substrate during deposition.

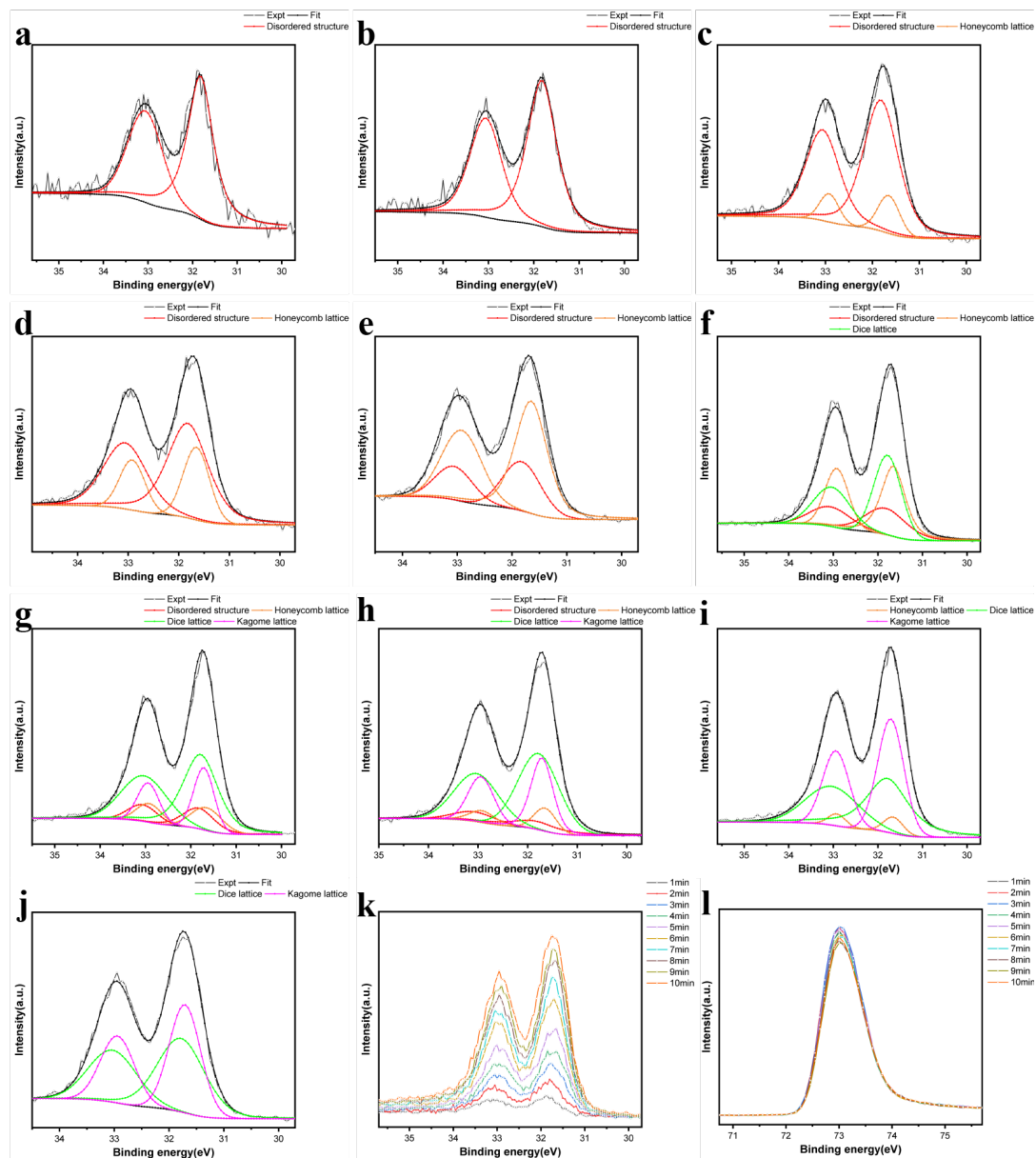


Figure. 2. Sb 4d and Al 2p core-level spectra as a function of deposition time exported by XPSpeak. (a)–(j) content changes of the disordered structure (red line), honeycomb lattice (blue line), dice lattice (green line), and kagome lattice (purple line) within 1–10 min deposition time; (k)–(l) core-level spectra of Sb 4d and Al 2p in different deposition times.

The spin-orbit coupling (SOC) effect causes the splitting of XPS peaks into

doublets. This effect is more pronounced in elements with larger atomic numbers. Therefore, the Sb 4d peak splits into Sb 4d_{3/2} and Sb 4d_{5/2} peaks due to SOC, with an area ratio of 2:3 between these peaks. Similarly, the Al 2p peak splits into Al 2p_{1/2} and Al 2p_{3/2} peaks. However, since the SOC effect of Al is less significant compared to Sb, the double-peak structure of Al 2p is not as prominent.

	disordered structure		Honeycomb lattice		Dice lattice		Kagome lattice	
	4d _{3/2}	4d _{5/2}	4d _{3/2}	4d _{5/2}	4d _{3/2}	4d _{5/2}	4d _{3/2}	4d _{5/2}
Binding energy	33.06	31.82	32.92	31.65	33.03	31.78	32.94	31.71
1min	326.5278	489.7916						
2min	610.5005	915.75						
3min	763.2236	1144.835	113.974	170.961				
4min	797.608	1196.412	320.6038	480.9057				
5min	402.7031	604.0547	899.5793	1349.369				
6min	390.3087	585.4631	677.9305	1016.896	709.636	1064.454		
7min	263.1233	394.6849	255.565	383.3475	1135.054	1702.581	461.0861	691.6292
8min	232.9268	349.3902	198.805	298.2075	1248.453	1872.68	687.08	1030.62
9min			136.741	205.1115	1336.741	2005.111	1295.148	1942.722
10min					1473.483	2210.225	1327.337	1991.006

Table 1. Increase in binding energy and peak area with deposition time. The area ratio of Sb 4d_{3/2} and Sb 4d_{5/2} is 2:3, and the binding energy in the same component is constant.

In the early stage of deposition (1-2 min), only one component was detected in the XPS spectra (disordered structure). Subsequently, the disordered structure vanished after 8 min. The honeycomb lattice appeared as deposition time increased (≥ 3 min). Further, with increasing deposition time (≥ 7 min), the kagome lattice in the form of nanometer-sized islands was formed over the dice lattices, all XPS fitting results are consistent with the STM measurements.

3. Results and discussion

Different phases of antimonene can be identified using STM, while only one type of RHEED pattern is observed, as shown in Figs. 1e and 1f. The diffraction patterns of both Al(111) and the Sb layer can be simultaneously visualized on the fluorescent screen. The 1/3 diffraction streaks correspond to three times the

interplanar spacing of $\{1\bar{1}0\}$ or $\{2\bar{1}\bar{1}\}$ in Al-single crystal, matching the lattice constants of 8.48Å and 4.90Å, respectively, as shown in Figs. 3b and 3c. These values are significantly larger than those of free-standing β -Sb.

Because of the high surface sensitivity of RHEED, rotating the sample stage to direct the electron beam grazing along different crystal directions allows for the determination of the sample's rotational symmetry. It is observed that antimonene epitaxially grown on the Al(111) surface shares the same rotational symmetry as the substrate; both can be described using the 2D plane group p6mm. Combined with the STM observations shown in Fig. 3e, it can be inferred that the antimonene lattice on the Al(111) substrate exists in a multilayered form, with upper and lower atoms arranged in a staggered manner, forming a layered stacking configuration. By stacking those layers of dice lattice in an "ABA" manner, as depicted in Fig. 3f, a new honeycomb structure is formed, as indicated by the black dashed line in Fig. 3f, which is considered to be β -Sb with a certain bending angle. Since STM can only observe the atomic arrangement of the outermost layer, this explained the lattice constants close to 1 nm appear in previous measurements. The adsorption site between kagome and dice lattice in Fig. 3i can be determined through the STM image presented in Fig. 3g. As a result, various phases of antimonene can be distinguished using STM, but each phase corresponds to only one type of RHEED pattern, as illustrated in Figs. 1e and 1f. Note that the dashed lines of top view between atoms in Fig. 3 only emphasize the arrangement and symmetry of atoms, and do not represent the type of chemical bonding or interaction between atoms.

First-principles calculations were performed using the projector augmented wave method [34] with the Perdew, Burke, and Ernzerhof functional [35] within the generalized gradient approximation (GGA) [36, 37], implemented in the Vienna ab initio simulation package (VASP) [38]. The cutoff energy of the plane-wave basis set was set to 600 eV. The relaxed calculations were performed using a Gaussian smearing scheme with Γ -Centered $7\times 7\times 1$ K -mesh. The convergence criteria for the total (free) energy change and the maximum force on each atom were set to 1×10^{-5} eV and 0.02 eV/Å, respectively.

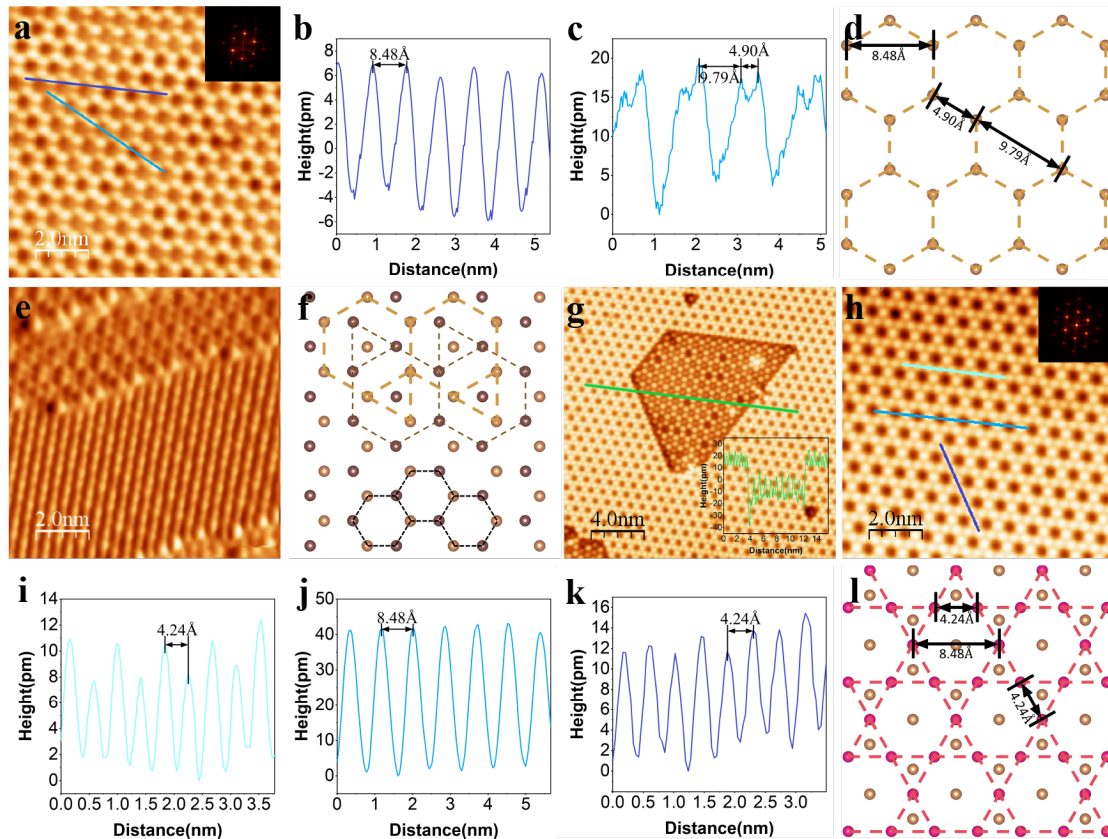


Figure 3. Structures of various phases of antimonene on the Al(111) surface ascertained by STM. (a) 10nm×10nm STM image of honeycomb lattice with $V_b=0.4\text{V}$ and $I_t=500\text{pA}$, and a Fast Fourier Transform (FFT) is included in the upper right corner. (b and c) Profile along indigo line and turquoise line in (a) indicate that the lattice constants of honeycomb structure are around 8.48Å, 9.79Å and 4.90Å respectively. (d) Top view of honeycomb lattice. (e) 10nm×10nm STM current image of Sb lattice under multilayered form with $V_b=0.5\text{V}$ and $I_t=600\text{pA}$ for 6 mins. (f) Top view of multiple repeated dice lattice with the upper (orange-colored atoms) and lower (brown-colored atoms) layers interwoven or offset in a specific, orderly fashion. (g) 20nm×20nm STM image of kagome lattice, dice lattice and honeycomb lattice simultaneous existence for 8 min deposition with $V_b=0.5\text{V}$ and $I_t=700\text{pA}$. Inset: A height profile along the green line, indicate the interplanar distance between kagome and dice lattice are around 10pm. (h) 10nm×10nm STM image of kagome lattice with $V_b=0.5\text{V}$ and $I_t=310\text{pA}$, and the FFT in the upper right corner. (i, j and k) Profile along aqua green, turquoise and indigo line in (a) indicate that the lattice constants of kagome structure are around 4.24Å, 8.48Å and 4.24Å respectively. (l) The kagome

lattice (pink layer) adsorbed on the bridge site of dice lattice layer (orange layer).

The properties of bonds in the lattice are determined by the chemical environment, and the electron localization function (ELF) [39] provides insight into the distribution of electron clouds between atoms [40] to ascertain the type of interaction. The ELF analysis in Fig. 4 shows the electron cloud around the Sb atoms are clearly concentrated between adjacent atoms, the regions of concentrated electron density connecting atomic centers suggest the formation of covalent bonds, and some bonds are polar covalent due to asymmetry in the electron cloud distribution, with the density skewed toward one of the atoms.

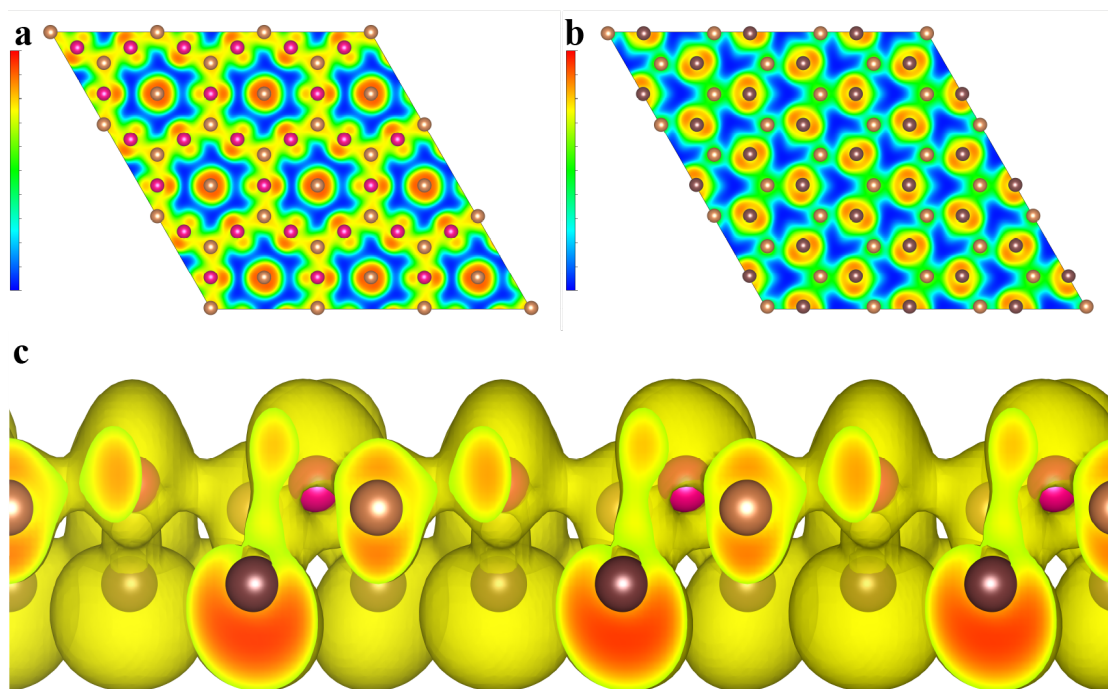


Figure. 4. ELF image exported by VESTA. (a and b) 2D plots of electron density distribution, and the color gradient (red to blue) indicate the distribution of electron clouds. (c) 3D isosurface plot of electron density around Sb atoms.

Both β -Sb and the kagome lattice share the $p6mm$ crystal point group, reflecting their sixfold rotational symmetry. Consequently, the same high-symmetry path was selected for the band structure calculations. The calculated electronic band structures

of β -Sb and the kagome lattice, obtained from static calculations, are presented in Figs. 5a and 5b, respectively. Notably, a Dirac point is observed below Fermi level at -1.38eV at the Γ point, which indicate that the β -Sb on Al(111) may exhibit non-trivial topological characteristics. Specifically, it could be a 2D topological insulator, where the bulk is insulating, but there are conducting edge states that are topologically protected. After incorporating SOC into the band structure calculations in Fig 5a, a band gap of 0.1712eV opens at the location of the original Dirac point.

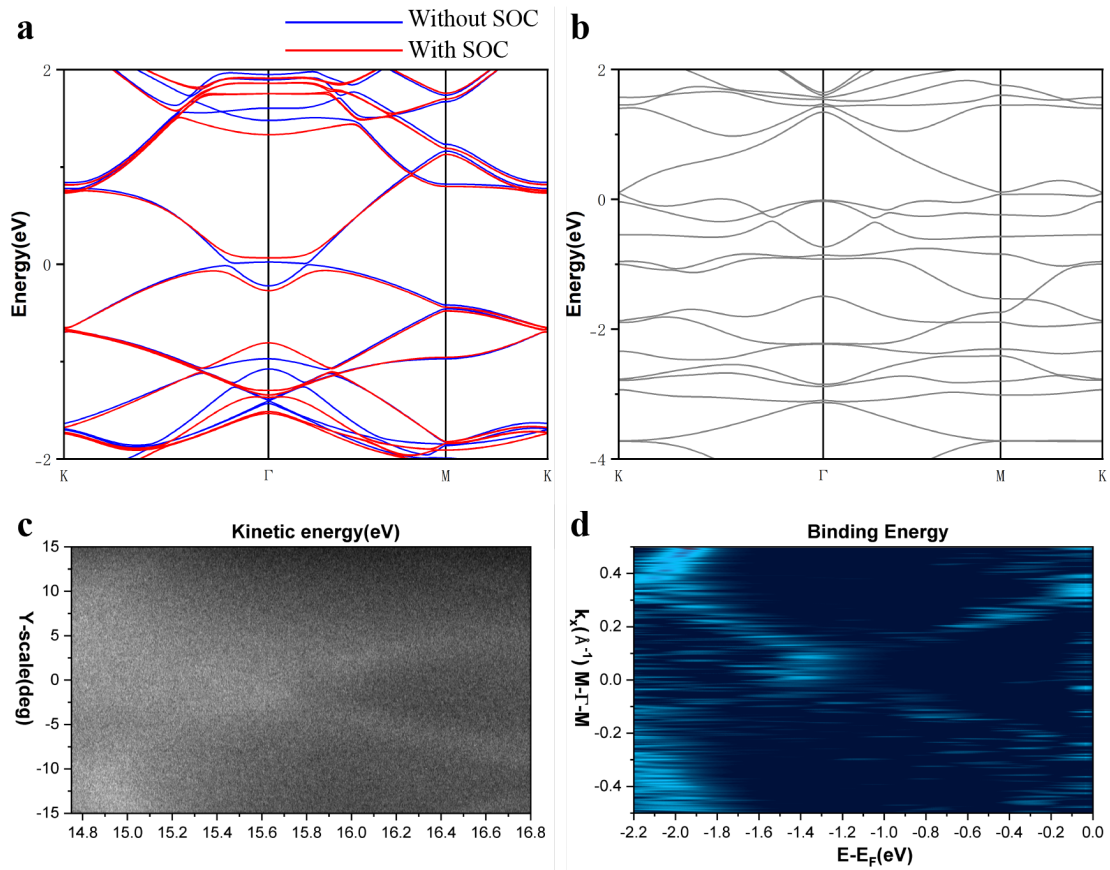


Figure 5. Electronic structures of honeycomb and kagome lattice. (a) and (b) show the band structure of honeycomb and kagome lattice respectively exported by vaspkit [41]. (c) Energy-dispersion spectrum in boundary state with $h\nu=21.218\text{eV}$, and the horizontal axis starts from 14.75eV . (d) $E-k$ relationships using 2D curvature method [42] exported by Igor.

According to Bloch's theorem [43], energy levels in isolated atoms convert into energy bands as electrons move coherently within the periodic potential of a crystal. The motion of electrons near the Fermi level, with high energy in the outermost shells,

typically results in a high degree of dispersion in the band structure and a lower density of states (DOS) than the more localized electrons in the inner shells. The lattice structure and quantum interference effects are crucial in determining the electron motion. In the case of confined fermions or bosons in a kagome lattice with only nearest-neighbor hopping, completely destructive quantum interference occurs. This leads to a flat dispersion relation for trapped particles [22]. Consequently, the energy of electrons near the Fermi level in Sb atoms, as shown in Fig. 5b, exhibits minimal variation with changes in the wave vector position, resulting in a low dispersion flat band (FB), that electrons have a highly localized characteristic that enhances their interaction effects with each other, leads to the display of unique behaviors in the electronic transport properties of FB systems, such as extremely high mobility, very low resistivity, strong correlation effects, and Wigner crystals [44].

To experimentally investigate the energy dispersion along the M - Γ - M direction, angle-resolved photoemission spectroscopy (ARPES) [45] measurements were conducted using an Omicron apparatus equipped with a He I light source at temperature of 7 K and pressure of 3×10^{-11} mbar. The ARPES spectrum in Fig. 5c remains consistent for deposition times less than 10 min, the band crossing at the Γ point below the Fermi level at around -1.4 eV shown in Fig. 5c are known as Dirac point. The linear relation of Dirac point results in highly conductive properties in boundary state [46]. The explanation for the occurrence of Dirac points in the honeycomb lattice can be provided by the Haldane model [47]. This model posits that the nontrivial topological properties of band structure originate from the breaking of time-reversal symmetry induced by next-nearest-neighbor hopping, and the experimental confirmation of Dirac points in graphene [48] further corroborated the Haldane model.

However, graphene in intrinsic state is limited in the applications of next-generation electronic devices due to its characteristic of having a zero band gap, in order to create a band gap, introducing SOC can presents a strategy. In contrast to graphene, antimonene exhibits a stronger SOC effect, manifesting as a double-peak split in the Sb 4d energy spectrum shown in Fig. 2. According to the Kane-Mele

model [49], the introduction of SOC leads to a non-zero Z_2 topological number in antimonene, thereby giving rise to special topological boundary states. The topological number of the band structure can be expressed as an integral along the boundaries of the first Brillouin zone. The opposite edges of the first Brillouin zone differ only by a reciprocal lattice vector. According to the Bloch theorem, this equivalence is reflected in the wave function, where the expression of electronic states between opposite edges differs by only a phase factor, satisfying U(1) gauge transformation [46].

In the case of trivial topology, the exponent of the phase factor remains constant. Therefore, when integrating along a closed loop throughout the Brillouin zone, the Chern number is zero. However, when the exponent of the phase factor between opposite edges varies with the position coordinates in reciprocal space, circling around the boundaries of the first Brillouin zone leads to non-cancellation of contributions between opposite edges, resulting in a non-zero topological number, indicating a non-trivial band structure that analogous to a Möbius strip [50], where after circling it, a phase difference exists. The singularity of the Möbius strip corresponds to the band structure at the Dirac point, shown as Fig. 5d. The consistent observation of a Dirac point at the same location in both experimental and theoretical studies indicates that the material likely possesses symmetry-protected Dirac states robust against spin-orbit coupling, suggesting it has non-trivial topological properties and potential applications in advanced quantum technologies.

In this context, the experimental results depicted in Figs. 5c and 5d first proved that antimonene on Al(111) behaves as a 2D topological insulator experimentally. It is worth mentioning that measuring the boundary state of a 2D topological insulator using ARPES is more challenging than measuring the surface state of a 3D topological insulator, such as the topological surface state of Bi_2Se_3 [51], due to the difficulty of obtaining ordered $E-k$ relationships from photoelectrons emitted from the edge of a 2D material. However, if the 2D material possesses well-defined atomic edge states, as illustrated in Figs. 1h and 1i, the measurement becomes feasible.

4. Conclusions

Various phases of antimonene, including the previously unpredicted kagome lattice structure, can be synthesized on an Al(111) substrate at room temperature without an alloy layer. ARPES measurements and DFT calculations reveal the presence of a Dirac cone below the Fermi level at approximately -1.4eV in the boundary state, first demonstrated that antimonene exhibits characteristics of 2D topological insulators in experimental, thereby offering great potential for developing next-generation electronic devices. Furthermore, DFT calculations also demonstrate the delocalization of electrons in kagome phase, corresponding to the FB structure with low dispersion near the Fermi level of antimonene on Al(111), and the FB structure enables the boundary states tend to emerge within the energy gap, making them robust against localized perturbations. In summary, antimonene on Al(111) represents a 2D topological insulator with a helical boundary modes and a low dispersion electronic structure near the Fermi level in the kagome phase.

AUTHOR DECLARATIONS

Conflict of Interest

The authors have no conflicts to disclose

Data availability

The data that support the findings of this research will be made available on request.

References

- [1] Novoselov K S, Geim A K, Morozov S V, Jiang D, Zhang Y, Dubonos S V, Grigorieva I V and Firsov A A, Electric Field Effect in Atomically Thin Carbon Films, 2004 *Science* [306 666–9](#)
- [2] Novoselov K S, Geim A K, Morozov S V, Jiang D, Katsnelson M I, Grigorieva I V, Dubonos S V and Firsov A A, Two-dimensional Gas of Massless Dirac Fermions in

- Graphene, 2005 *Nature* **438** 197–200
- [3] Kane C L and Mele E J, Quantum Spin Hall Effect in Graphene, 2005 *Phys Rev Lett.* **95** 226801
- [4] Wang J-Y, Deng S-B, Liu Z-F and Liu Z-R, The Rare Two-dimensional Materials with Dirac Cones, 2005 *Natl Sci Rev.* **2** 22–39
- [5] Zhang S-L, Xie M-Q, Li F-Y, Yan Z, Li F-Y, Kan E, Liu W, Chen Z-F and Zeng H-B, Semiconducting Group 15 Monolayers: A Broad Range of Band Gaps and High Carrier Mobilities, 2016 *Angew. Chem. Int. Ed.* **55** 1666–9
- [6] Li L-K, Yu Y-J, Ye G-J, Ge Q-Q, Ou X-D, Wu H, Feng D-L, Chen X-L and Zhang Y-B, Black Phosphorus Field-effect Transistors, 2014 *Nat Nanotechnol.* **9** 372–7
- [7] Zhang J-L, Zhao S-T, Han C, Wang Z-Z, Zhong S, Sun S, Guo R, Zhou X, Gu C-D and Yuan K-D, *et al*, Epitaxial Growth of Single Layer Blue Phosphorus: A New Phase of Two-Dimensional Phosphorus, 2016 *Nano Lett.* **16** 4903–8
- [8] Zhang S-L, Yan Z, Li Y-F, Chen Z-F and Zeng H-B, Atomically Thin Arsenene and Antimonene: Semimetal-semiconductor and Indirect-direct Band-gap Transitions. 2015 *Angew, Chem. Int. Ed.* **54** 3112–5
- [9] Carrasco J S, Congost-Escoín P, Assebban M and Abellán G, Antimonene: a tuneable post-graphene material for advanced applications in optoelectronics, catalysis, energy and biomedicine. 2023 *Chem. Soc. Rev.* **52** 1288–330
- [10] Reis F, Li G, Dudy L, Bauernfeind M, Glass S, Hanke W, Thomale R, Schäfer J and Claessen R, Bismuthene on a SiC Substrate: A Candidate for a New High-temperature Quantum Spin Hall Material, 2017 *Science* **357** 287–90
- [11] Wang G-X, Pandey R and Karna S P, Atomically Thin Group V Elemental Films: Theoretical Investigations of Antimonene Allotropes, 2015 *Acs Appl Mater.* **7** 11490–6
- [12] Ji J-P, Song X-F, Liu J-Z, Yan Z, Huo C-X, Zhang S-L, Su M, Liao L, Wang W-H, Ni Z-H, Hao Y-F and Zeng H-B, Two-dimensional Antimonene Single Crystals Grown by van der Waals Epitaxy, 2016 *Nat Commun.* **7** 13352–60
- [13] Shao Y, Liu Z-L, Cheng C, Wu X, Liu H, Liu C, Wang J-O, Zhu S-Y, Wang Y-Q, Shi and D-X, *et al*, Epitaxial Growth of Flat Antimonene Monolayer: A New Honeycomb Analogue of Graphene, 2018 *Nano Lett.* **18** 2133–9
- [14] Zhu S-Y, Shao Y, Wang E, Cao L, Li X-Y, Liu L-Z, Liu C, Liu L-W, Wang J-O, Ibrahim O, Sun J-T, Wang Y-L, Du S-X and Gao H-J, Evidence of Topological Edge States in Buckled Antimonene Monolayers, 2019 *Nano Lett.* **19** 6323–9
- [15] Cantero E D, Martínez E A, Serkovic-Loli L N, Fuhr J D, Grizzi O and Sánchez E A, Synthesis and Characterization of a Pure 2D Antimony Film on Au(111), 2021 *J. Phys. Chem. C.* **125** 9273–80
- [16] Sun S, Yang T, Luo Y-Z, Gou J, Huang Y-L, Gu C-D, Ma Z-R, Lian X, Duan S-S and Andrew T S W, *et al*, Realization of a Buckled Antimonene Monolayer on Ag(111) via Surface Engineering, 2020 *J Phys Chem Lett.* **11** 8976–82
- [17] Zhang P, Ma C, Sheng S-X, Liu H, Gao J-S, Liu Z-J, Cheng P, Feng B-J, Chen L and Wu K-H, Absence of topological β -antimonene and growth of α -antimonene on noble metal Ag(111) and Cu(111) surfaces, 2022 *Phys. Rev. Mater.* **6** 074002
- [18] Radha S K and Lambrecht W R L, Topological Band Structure Transitions and Goniopolar Transport in Honeycomb Antimonene as a Function of Buckling, 2020 *Phys*

Rev B. **101** 235111

- [19] Zhao M-W, Zhang X-M and Li L-Y, Strain-driven Band Inversion and Topological Aspects in Antimonene, 2015 *Sci Rep.* **5** 16108
- [20] Hasan M Z and Kane C L, Colloquium: Topological Insulators, 2010 *Rev Mod Phys.* **82** 3045–67
- [21] Sun K, Gu Z-C, Katsura H and Sarma S D, Nearly Flatbands with Nontrivial Topology, 2011 *Phys Rev Lett.* **106** 236803
- [22] Li Z, Zhuang J-C, Wang L, Feng H-F, Gao Q, Xu X, Hao W-C, Wang X-L, Zhang C and Wu K-H, et al, Realization of Flat Band with Possible Nontrivial Topology in Electronic Kagome Lattice, 2018 *Sci Adv.* **4** eaau4511
- [23] Kubo O, Kinoshita S, Sato H, Miyamoto K, Sugahara R, Endo S, Tabata H, Okuda T and Katayama M, Kagome-like Structure of Germanene on Al(111), 2021 *Phys Rev B.* **104** 085404
- [24] Sassaa A, ohanssonb F O L, Lindbladb A, Yazdic M G, Simonovb K, Weissenriederc J, and Muntwilerd M, Iyikanate F, Sahinf H, and Angotg T, *et al*, Kagome-like Silicene: A Novel Exotic Form of Two-dimensional Epitaxial Silicon, 2020 *Appl Surf Sci.* **530** 147195
- [25] Derivaz M, Dentel D, Stephan R, Hanf M C, Mehdaoui A, Sonnet P and Pirri C, Continuous Germanene Layer on Al(111), 2015 *Nano lett.* **15** 2510–6
- [26] Wintterlin J, Wiechers J, Brune H, Gritsch T, Höfer H and Behm R J, Atomic-resolution Imaging of Close-packed Metal Surfaces by Scanning Tunneling Microscopy, 1989 *Phys Rev Lett.* **62** 59–62
- [27] Binnig G and Rohrer H, Scanning Tunneling Microscopy, 2000 *IBM J. Res. Develop.* **44** 279–93
- [28] Peng L-M, Dudarev S L and Whelan M J, Electron Scattering Factors of Ions and Dynamical RHEED From Surfaces of Ionic Crystals, 1998 *Phys Rev B.* **57** 7259–65
- [29] Shukla, A K, Banik S, Dhaka R S, Biswas C, Barman S R and Haak H, Versatile UHV Compatible Knudsen Type Effusion Cell, 2004 *Rev Sci Instrum.* **75** 4467–70
- [30] Wang Y-L and Ding Y, Electronic Structure and Carrier Mobilities of Arsenene and Antimonene Nanoribbons: A First-Principle Study, 2015 *Nanoscale Res Lett.* **10** 254–64
- [31] Kotecký R, Salas J and Sokal A D, Phase Transition in the Three-State Potts Antiferromagnet on the Diced Lattice, 2008 *Phys Rev L.* **101** 030601
- [32] Morgan D J, Metallic antimony (Sb) by XPS, 2017 *Surf. Sci. Spectra.* **24** 024004
- [33] McCafferty E and Wightman J P, Determination of the concentration of surface hydroxyl groups on metal oxide films by a quantitative XPS method, 1998 *Surf Interface Anal.* **26** 549–64.
- [34] Perdew J P, Burke K and Ernzerhof M, Generalized Gradient Approximation Made Simply, 1996 *Phys Rev Lett.* **77** 3865–8
- [35] BlöchlA P E, Projector Augmented-wave Method, 1994 *Phys Rev B Condens Matter.* **50** 17953–79
- [36] Perdew J P, Chevary J A, Vosko S H, Jackson K A, Pederson M R, Singh D J and Fiolhais C, Atoms, Molecules, Solids, and Surfaces: Applications of the Generalized Gradient Approximation for Exchange and Correlation, 1993 *Phys Rev B.* **46** 6671–87
- [37] Langreth C D and Mehl M J, Beyond the Local-density Approximation in Calculations of

- Ground-state Electronic Properties, 1983 *Phys Rev B*. **28** 1809–34
- [38] Kresse G, Ab initio Molecular Dynamics for Liquid Metals, 1995 *J Non-cryst Solids*. **192**, **193** 222–9
- [39] De Santis L and Resta R, Electron Localization at Metal Surfaces, 2000 *Surf Sci*. **450** 126–32
- [40] Becke A D and Edgecombe K E, A Simple Measure of Electron Localization in Atomic and Molecular Systems, 1990 *J. Chem. Phys.* **92** 5397–403
- [41] Wang V, Xu N, Liu J-C, Tang G and Geng W T, VASPKIT: A User-friendly Interface Facilitating High-throughput Computing and Analysis Using VASP Code, 2019 *Comput Phys Commun*. **267** 108033
- [42] Zhang P, Richard P, Qian T, Xu Y-M, Dai X and Ding H, A Precise Method for Visualizing Dispersive Features in Image Plots, 2011 *Rev Sci Instrum*. **82** 043712
- [43] Bloch V F, über die Quantenmechanik der Elektronen in Kristallgittern, 1928 *ZS. f. Phys.* **52** 555–99
- [44] Wu C, Bergman D, Balents L and Das Sarma S, Flat Bands and Wigner Crystallization in the Honeycomb Optical Lattice, 2007 *Phys Rev Lett*. **99** 070401
- [45] Damascelli A, Probing the Electronic Structure of Complex Systems by ARPES, 2004 *Phys Scr*. **T109** 61–74
- [46] Ando Y, Topological Insulator Materials, 2013 *J Phys Soc Jpn*. **82** 102001
- [47] Haldane F D M, Model for a Quantum Hall Effect without Landau Levels: Condensed-Matter Realization of the "Parity Anomaly", 1988 *Phys Rev Lett*. **61** 2015–8
- [48] Zhang Y-B, Tan Y-W, Stormer H L and Kim P, Experimental observation of the quantum Hall effect and Berry's phase in graphene, 2005 *Nature* **438** 201–4
- [49] Kane C L and Mele E J, Z_2 Topological Order and the Quantum Spin Hall Effect, 2005 *Phys Rev Lett*. **95** 146802
- [50] Hari C. M, Topological Insulators: A Romance with Many Dimensions, 2010 *Nat. Nanotechnol*. **5** 477–9
- [51] Kim S, Ye M, Kuroda K, Yamada Y, Krasovskii E E, Chulkov E V, Miyamoto K, Nakatake M, Okuda T and Ueda Y, *et al*, Surface Scattering via Bulk Continuum States in the 3D Topological Insulator Bi_2Se_3 , 2011 *Phys Rev Lett*. **107** 056803